ACS APPLIED MATERIALS & INTERFACES

Research Article

www.acsami.org

Effect of Chemical Modification of Graphene on Mechanical, Electrical, and Thermal Properties of Polyimide/Graphene Nanocomposites

Hun Wook Ha,[§] Arup Choudhury,[§] Tahseen Kamal, Dong-Hun Kim, and Soo-Young Park*

Department of Polymer Science & Engineering, Kyungpook National University, #1370 Sankyuk-Dong, Buk-gu, Daegu 702-701, Republic of Korea

ABSTRACT: Chemically modified graphene sheets were dispersed in a high-performance polyimide (PI) matrix using polyamic acid (PAA)/graphene nanocomposite as a precursor. PI nanocomposite films with different loadings of graphene sheets were prepared by thermal imidization of the as-prepared PAA/graphene nanocomposites. Graphene oxide (GO) synthesized by Hummer's method was chemically reduced with various reducing agents to produce reduced GOs (rGOs). The incorporation of only 5 wt % GO resulted in an ~12-fold and ~18-fold increase in the tensile strength and tensile modulus of PI, respectively, while the PI/rGO nanocomposites were found to have relatively inferior tensile properties. The superior mechanical properties of the PI/GO nanocomposites were attributed to the good dispersion and effective stress transfer between the polymer and GO sheets, as evidenced by the results from X-ray diffraction (XRD) and morphological studies. Furthermore, the PI/GO nanocomposites exhibited higher loading capacity than PI/rGO. The thermo-oxidative stability of PI was also remarkably improved with the addition of both GO and rGOs, but rGOs had a more pronounced effect. The electrical conductivity of PI/rGO nanocomposites was higher than that of PI/GO, suggesting restoration of the graphene basal plane upon the reduction of GO. The highest electrical conductivity was achieved for the L-ascorbic acid reduced GO-reinforced PI nanocomposites.

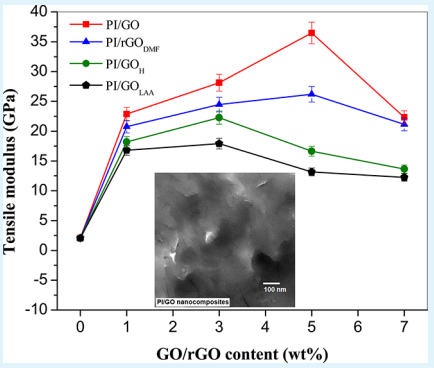

KEYWORDS: *nanocomposites, photoelectron spectroscopy (XPS), transmission electron microscopy (TEM), mechanical properties, thermal properties, electrical properties*

1. INTRODUCTION

Polymer-based nanocomposites have attracted considerable research interest in recent years, with the objective of obtaining high-performance materials. The incorporation of nanofillers such as carbon nanotubes and clay nanosheets into polymer matrix has satisfactorily enhanced both the mechanical and thermal properties of the resultant nanocomposites at a small loading.[1−3] In recent years, there has been great interest in using graphene-based nanofillers, such as graphite nanoplatelets (GNPs), graphene sheets (GS), and graphene oxide (GO), to fabricate a new class of advanced polymer composites[3−6] because of their unique mechanical[7] and thermal[8] properties. However, most of the recent studies on graphene−polymer composite materials have explored the improvement of polymer properties by the incorporation of GO. GO can be synthesized by several methods[9] and has a larger interlayer spacing than graphite, along with various oxygen functional groups (e.g., carbonyl, hydroxyl, and epoxide groups) on the basal planes and edges. These structural features facilitate the exfoliation of GO into individual single layers in water and polar organic solvents at lower concentrations. The reduction of GO is considered as a large-scale method for the production of the modified graphene nanofiller for use in polymer nanocomposites. GO can be exfoliated and reduced through liquid-phase chemical reduction,[10] thermal shocking,[11] and microwave treatment[12] to generate loosely stacked structures with a large specific surface area. The ease of processability and solubility of modified graphene sheets can be exploited in the design of advanced materials, such as thermally and mechanically enhanced polymer-based nanocomposites. However, the control of interfacial interaction between the graphene fillers and polymer for homogeneous dispersion is essential for achieving the required performance of the resulting nanocomposite materials. Shen et al.[13] prepared poly(vinyl alcohol) (PVA)/GO nanocomposites with an increase in tensile strength from 23 MPa to 49.5 MPa at a GO loading of 3.5 wt %, and the decomposition temperature of PVA was increased by 8 °C with the incorporation of 0.5 wt % GO. Salavagione et al.[14] reported a significant increase in the thermal stability of PVA/GO composites after chemical treatment with hydrazine. Wang et al.[15] achieved 21% increase in tensile strength and 24% increase in storage modulus for 2 wt % graphene-reinforced poly(butylene succinate) nanocomposites, compared to the pure polymer. Rafiee et al.[16] reported that a low content of thermally reduced GO showed better mechanical properties of the epoxy nanocomposites than

Received: June 4, 2012
Accepted: August 28, 2012
Published: August 28, 2012

   dx.doi.org/10.1021/am300999g | ACS Appl. Mater. Interfaces 2012, 4, 4623−4630

Scheme 1. Preparation of Polyamic Acid (PAA) and PI/rGO Nanocomposites

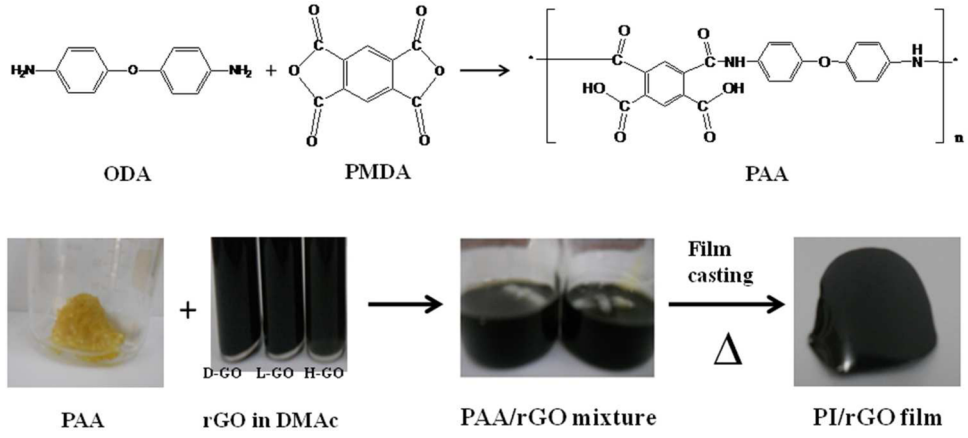

carbon nanotubes. Layek et al.[17] prepared PMMA/graphene nanocomposites by atom transfer radical polymerization (ATRP), followed by hydrazine reduction and found 124%, 157%, and 321% increases in storage modulus, stress at break, and tensile modulus, respectively, compared to those of the pure polymer. The tensile modulus of poly(styrene-*co*-acrylonitrile) was remarkably improved by reinforcement with chemically reduced GO, compared to that of graphite.[18]

Polyimides (PIs) belong to an important class of thermoplastics, because of their high glass-transition temperature, good chemical stability, excellent mechanical properties, and outstanding thermal and thermo-oxidative stability. These key properties have led to the widespread use of PI in a range of electronic and aerospace applications. With the development of nanotechnology, PI-based nanocomposites with inorganic nanofillers such as metal nanoparticles,[19,20] layered silicate compounds,[21,22] and synthetic clays[23,24] have been explored to further improve the properties of PI materials. The inclusion of carbon nanotubes (CNTs) to PI matrices has already been shown to improve their mechanical, electrical, and thermal properties.[25−27] However, there are some fundamental issues related to the dispersion, alignment, and interfacial adhesion, which have partly limited the development of high-quality composite materials. In this regard, the discovery of graphene has opened up a new opportunity to introduce it to PI matrices for developing PI-based nanocomposites with superior properties. Recently, a few researchers have used graphene oxide and functionalized graphene nanofillers to improve the mechanical thermal and electrical properties of PI.[28−32]

In this study, we demonstrated an effective approach for the fabrication of PI-based nanocomposites with exfoliated GO and rGO sheets by using PAA/GO or PAA/rGO nanocomposites as the precursors, because the possible noncovalent interactions between functional groups of the GO/rGO and that of the PAA could suppress the phase separation during the thermal imidization process. The prepared PI/graphene nanocomposite films exhibit a remarkable enhancement of mechanical, thermal, and electrical properties, indicating uniform dispersion of the GO/rGO sheets in the PI matrix.

2. EXPERIMENTAL SECTION

2.1. Materials. Pyromellitic dianhydride (PMDA) obtained from Sigma−Aldrich was dried under vacuum at 120 °C prior to use. 4,4-Oxidianiline (ODA) and dimethylacetamide (DMAc) were used as received from Sigma−Aldrich. Graphite (particle size = 20−25 μm, purity = 99.95%) was used as received from Samjung C&G Inc., Korea. Sulfuric acid (H_2SO_4), hydrochloric acid (HCl), hydrogen peroxide (H_2O_2), potassium permanganate ($KMnO_4$), and sodium nitrate ($NaNO_3$) were purchased from Sigma−Aldrich. Hydrazine hydrate ($N_2H_4{\cdot}H_2O$) (85%), L-ascorbic acid (LAA) and *N*,*N*-dimethylformamide (DMF) were procured from Junsei Chemical Co., Japan.

2.2. Preparation of Graphene Oxide (GO) and Reduced Graphene Oxide (rGO). GO was synthesized by the oxidation of graphite using the modified Hummers method.[33] Briefly, 4 g of raw graphite, 2 g of $NaNO_3$, and 12 g of $KMnO_4$ were added to a 500-mL round-bottom flask containing 100 mL concentrated H_2SO_4. The mixture was first cooled by immersion in an ice bath for 1 h with constant stirring and then slowly heated to 35 °C for 3 h before being terminated by the addition of 200 mL of deionized (DI) water. After 30 min, a 30% H_2O_2 solution (3 mL) was added to the mixture to reduce the unreacted permanganate. The mixture was filtered through a membrane filter (0.2 μm pore size) and washed with dilute HCl and DI water. The resulting GO was then dried at 40 °C for 48 h.

The synthesized GO was chemically reduced using different reducing agents such as anhydrous DMF, LAA, and N_2H_4. In a typical reduction by DMF,[34] 50 mg of GO was dispersed in 100 mL of DMF by ultrasonication (Sonic Vibracell, VCX-750, 60 Hz) for 30 min. The mixture was then heated in an oil bath at 153 °C for 1 h. The resulting suspension was filtered through a membrane filter and washed repeatedly with DI water to remove the excess DMF. Finally, the DMF-reduced GO (rGO_D) was dried under vacuum.

In the reduction procedure of GO by hydrazine hydrate, the as-prepared GO was dispersed in water with ultrasonic treatment. Two milliliters (2 mL) of N_2H_4 was then immediately added to 200 mL of aqueous GO suspension, and the resulting mixture was heated in an oil bath to 100 °C for 12 h, followed by the precipitation of rGO as a black solid. The hydrazine-reduced GO (rGO_H) was filtered, washed with water, and dried.

Reduction of GO by LAA was performed as follows: 20 mg GO was first dispersed in 200 mL of water with ultrasonication for 1 h, and then 200 mg of LAA was added to the resulting suspension with constant stirring and ultrasonication for 30 min, followed by heating in an oil bath at 80 °C for 24 h. The mixture was cooled to room temperature and sonicated for 1 h. LAA-reduced GO (rGO_L) powder was obtained after filtration, washing, and drying.

2.3. Preparation of PI Nanocomposites with GO and rGO. Pure PI and PI-based nanocomposites containing various concentrations of GO or rGOs were prepared using a conventional solution casting method and subsequent thermal imidization. To synthesize PAA, 2 g of ODA was first completely dissolved in 40 mL of DMAc by mechanical stirring. PMDA (2.16 g) was then added to the ODA solution, and the mixture was stirred at room temperature in a N_2-purged glovebox for 24 h. Subsequently, a viscous PAA solution was poured into methanol to precipitate PAA, followed by drying to obtain pure PAA. To prepare the PAA/GO composite solution, the pure PAA

was diluted by the mixture of DMAc and GO/DMAc (1 mg mL^{-1}) suspension. For instance, 1 g of pure PAA was mixed with 5 mL of GO suspension and 5 mL of DMAc by sonication for 6 h and mechanical stirring for 12 h to obtain a PAA/GO (1 wt %) solution. The precursor solution was poured onto a clean glass plate and a film was cast by drawing a glass bar over the plate. The separation between the glass bar and plate—and, hence, the film's thickness—was controlled by the thickness of tape rolled on both ends of the glass bar. The as-cast film was initially dried in a dry air-flowing oven at 60 °C for 10 h to remove most of the solvent. The nanocomposite film was then heated to temperatures of 100, 150, 200, 250, and 300 °C for 1 h each and at 350 °C for 30 min to achieve full imidization. Finally, the films were cooled to room temperature and peeled from the glass plate to obtain the PI/GO nanocomposite films (~20 μm thick). A series of nanocomposite films with different GO and rGO contents (i.e., 1, 3, 5, and 7 wt %) was prepared using the above approach. The preparation of PAA and PI/rGO nanocomposites is presented in Scheme 1.

2.4. Characterization. X-ray photoelectron spectroscopy (XPS) (VG Microtech 2000 ESCA) was performed using a monochromatized Al Kα X-ray source (1486.6 eV). Wide-angle X-ray diffraction was carried out with an Anton-Parr X-ray generator (Cu K_α radiation with λ = 1.54 Å), using an accelerated voltage of 40 kV and a current of 40 mA. The morphology of the nanocomposite samples was studied by field emission scanning electron microscopy (FE-SEM) (Hitachi Model S-4800) with an acceleration voltage of 15 kV, and transmission electron microscopy (JEOL Model JEM 2100–2100F) operated at 200 kV. Cryogenically fracture surfaces of the nanocomposite samples were sputtered with gold prior to SEM analysis. Thin sections for the TEM observations were cut from the as-prepared nanocomposites using a Leica ultramicrotome with a diamond knife. The thermal stability and temperature variation of weight loss were measured by thermogravimetric analysis (SETARAM, TGA-DSC EVO) in a nitrogen atmosphere with a scan rate of 5 °C min^{-1} within the temperature range of 100–1000 °C. Tensile tests of the film samples were carried out using an Instron universal tensile test system, and the samples were directly mounted to the sample clamps with a crosshead speed of 5 mm min^{-1}. The electrical conductivity (σ) was measured using a four-point probe (Ecopia HMS-3000 electrometer) and calculated from the equation

$$\sigma\ (\mathrm{S/cm}) = \frac{1}{tR_s}$$

The sample thickness (t) and sheet resistance (R_s) were measured using calipers and a four-point probe, respectively.

3. RESULTS AND DISCUSSIONS

3.1. XPS Analysis. XPS study was performed to confirm the interaction between the filler and matrix in PI/GO or rGO nanocomposites. The N 1s binding energies of the PI/GO and PI/rGO nanocomposites, as well as their differences, compared to pure PI, were determined to monitor the PI–graphene interactions. Figure 1 shows the N 1s XPS spectra of the pure PI and its nanocomposites with 3 wt % GO, rGO_D, rGO_H, and rGO_L. The N 1s spectrum of pure PI exhibits an intense symmetrical peak centered at 401.1 eV, assigned to the imide (C–N) group.[35] After incorporation of graphene sheets into PI, the chemical environment of the N atom was changed, as shown by the broadening and shifting to lower binding energies of the N peak of the nanocomposites (see Figure 1). The magnitude of the changes in the binding energies of N 1s correlates with the strength of the interaction. The binding energy shift of 1.4 eV for PI/GO nanocomposites (399.7 eV) is slightly higher than that of 0.9 eV observed for the PI/rGO_L nanocomposites (400.2 eV), indicating that the interaction in the PI/GO nanocomposite is stronger than that in PI/rGO_L. The shifting of binding energies for PI/rGO_D and PI/rGO_H nanocomposites are 1.12 and 0.98, respectively. The broadening of the N 1s peak of the nanocomposites is possibly due to the presence of a new type of nitrogen moiety, which could be identified as a N atom (at the polar end group of PI) involved in a noncovalent interactions, such as van der Waals attraction force or hydrogen bonding,[30] with chemically modified graphene surface. The strong interaction between graphene sheets and PI matrix appears to have a beneficial impact on the mechanical properties of the resulting nanocomposites.

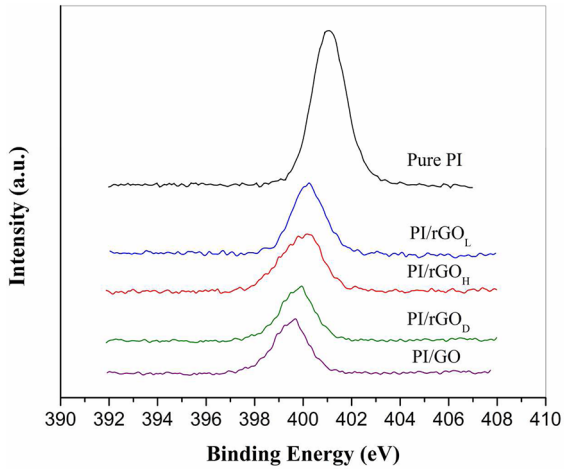

Figure 1. N 1s XPS spectra of pure PI and its nanocomposites with 3 wt % GO, rGO_D, rGO_H, and rGO_L loading.

3.2. Wide-Angle X-ray Diffraction. Figure 2 shows the two-dimensional (2D) wide-angle X-ray patterns of pure PI, PI/GO, and different PI/rGO nanocomposites. The innermost reflection at 2θ = 5.7° (d-spacing of 15.0 Å) was clearly observed for all samples. This d-spacing value was close to the calculated 15.4 Å repeat unit spacing along the axis of a fully extended chain, so that the reflection could be indexed as 002, based on a two-chain orthorhombic unit cell with dimensions a = 0.836 nm, b = 0.563 nm, and c = 3.303 nm, proposed by Liu et al.[36] The middle broad reflection at 2θ = 17° was due to the amorphous portion of the material. The outermost reflection at 2θ = 26.5° was very weak and broad. It could be the reflection from the 002 planes of the stacked graphene layers with a spacing of 0.34 nm. However, the broadness of this reflection indicates that the number of stacked graphene layers was small (around two or three stacks from peak width) and almost exfoliated, consistent with TEM results (see Figure 4, shown later in this work).

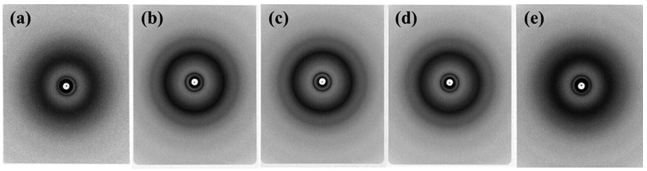

Figure 2. Two-dimensional (2D) wide-angle X-ray patterns of (a) PI, (b) PI/GO (3 wt %), (c) PI/rGO_D (3 wt %), (d) PI/rGO_H (3 wt %), and (e) PI/rGO_L (3 wt %).

3.3. Morphological Study. Figure 3 shows SEM images of the fractured cross section of pure PI and PI/GO or rGO nanocomposites with a loading of 3 wt %. As shown in SEM images of the nanocomposites, most of the graphene sheets are fully exfoliated and clearly well-dispersed in the PI matrix (see Figures 3b and 3c), whereas the pure PI film possess a smooth

dx.doi.org/10.1021/am300999g | ACS Appl. Mater. Interfaces 2012, 4, 4623–4630

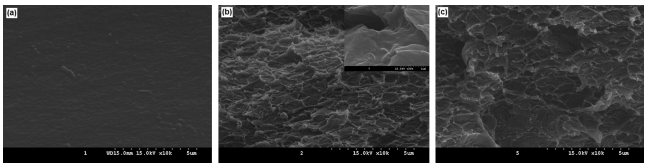

Figure 3. SEM images of cryogenically fractured cross-section of (a) pure PI, (b) PI/3 wt % GO, and (c) PI/3 wt % rGO_L nanocomposites.

fracture surfaces (see Figure 3a). The image also reveals that the graphene sheets are well-wrapped in or covered with a thick PI layer (see inset of Figure 3b). This could be attributed to the strong interfacial adhesion induced by the surface functional groups of GO, as well as the good compatibility between the PI matrix and GO sheets. Such strong interfacial bonding likely favors efficient stress transfer from the polymer matrix to the graphene sheets and thus enhanced mechanical properties of the nanocomposites. The graphene sheets are not just aligned parallel to the surface of the sample film, rather distributed randomly in the PI matrix. SEM images in Figure 3b and 3c demonstrate that there is no significant difference in the level of filler dispersion or exfoliation between the GO and rGO-filled nanocomposites. Figure 4a and 4b shows TEM images of the

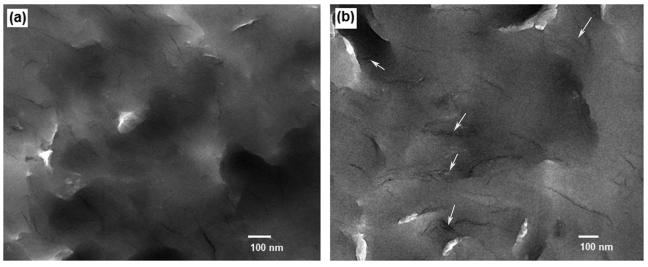

Figure 4. TEM images of microtomed cross sections of the PI nanocomposites with loadings of 3 wt %: (a) GO and (b) rGO_L.

microtomed cross sections of the PI nanocomposites with a 3 wt % GO and rGO_L loading, respectively. The TEM image of the PI/GO nanocomposites showed graphene sheets with an average thickness of 10 nm that are well-exfoliated and homogeneously dispersed over the PI matrix with almost no large agglomerates. This morphology is very consistent with the SEM observations. The good dispersion of GO sheets could be attributed to the good interaction between the oxygen functionalities on the GO surface and the polar groups of the PI matrix. On the other hand, the rGO-filled nanocomposite appeared to show a higher number of multilayer sheets with a large average thickness (21 nm) (lower aspect ratio) (Figure 3b), suggesting that the reduction process leads to the restacking of graphene sheets.

3.4. Mechanical Properties. The effect of pristine GO and reduced GO on the tensile properties of PI-based nanocomposites was studied. Figure 5 presents typical stress−strain curves for the pure PI, PI/GO and different PI/rGO nanocomposite films. Figure 6 shows the variations of tensile strength, tensile modulus, and percent elongation at break, as a function of the GO/rGO content. The mechanical properties of the pure PI and formulated PI/GO and PI/rGOs nanocomposites are tabulated in Table 1. Pure PI possesses a tensile strength of 120.3 MPa, a tensile modulus of 2.07 GPa, and an elongation at break of 32.6%. The incorporation of GO and rGO into PI films remarkably enhanced their tensile strength

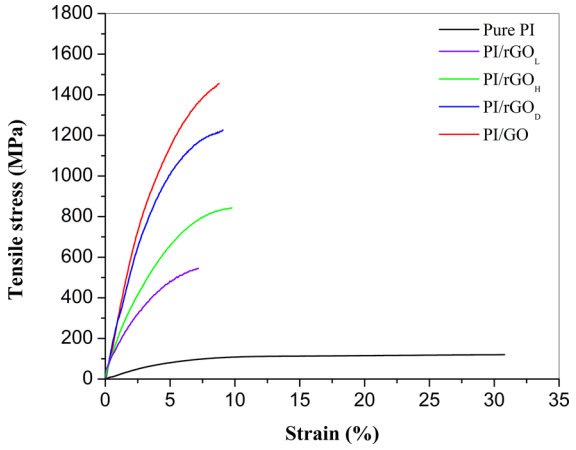

Figure 5. Typical stress−strain curves of pure PI and its nanocomposites with 5 wt % GO and rGOs.

and tensile modulus. For instance, the incorporation of 5 wt % GO increased the tensile strength and tensile modulus to 1456.8 MPa and 36.46 GPa, respectively, corresponding to increases of ~12 and ~18 times higher than that of the pure PI, respectively. The enhancement of tensile strength and modulus of the PI/GO nanocomposites could be attributed to the uniform dispersion of GO sheets in the PI matrix, as observed by TEM (Figure 4), thereby allowing an efficient stress transfer from the polymer matrix to the filler. Moreover, the noncovalent interaction (e.g., van der Waals attraction force or hydrogen bonding) between the functional groups of GO and PAA suppressed phase separation during the thermal imidization of PAA, maximizing the polymer reinforcing efficiency of GO to produce nanocomposites with superior performance. However, the good dispersion of GO within the PI matrix and the strong PI-GO interfacial interaction restrained the free movement or mobility of the PI macromolecular segments during extension, which decreased the elongation at break of the nanocomposite films. The tensile strength of the PI/GO nanocomposites increased from 1025 to 1456.8 MPa (42% increase) as the GO content increased from 1 wt % to 5 wt %. However, a further increase in the GO content to 7 wt % resulted in a decrease in tensile strength (to 1118 MPa). The tensile modulus of the PI/GO nanocomposites exhibited an identical trend to that of the tensile strength (see Figure 6). As the GO content increased from 1 wt % to 5 wt %, the tensile modulus increased from 22.87 GPa to 36.46 GPa, followed by a decrease to 22.32 GPa at a GO content of 7 wt %. Such a decrease in the tensile properties at higher GO loading (7 wt %) might be due to the increasing aggregation tendency of the GO layers forming some defects in the nanostructure of the nanocomposites. It can be noted that the enhancement of tensile strength and tensile modulus observed for the present PI/GO (5 wt %) nanocomposite films are larger than those of the previously reported values.[31,37] In contrast to earlier work, the different polymer structure obtained using PMDA as a monomer and the additional purification of PAA during the preparation of nanocomposites might result superior mechanical properties of the nanocomposites. For the unpurified PAA, the evaporation of residual monomer/oligomer molecules during high-temperature curing could form small voids/holes inside the nanocomposite materials, and consequently deteriorate the mechanical properties of the nanocomposites.

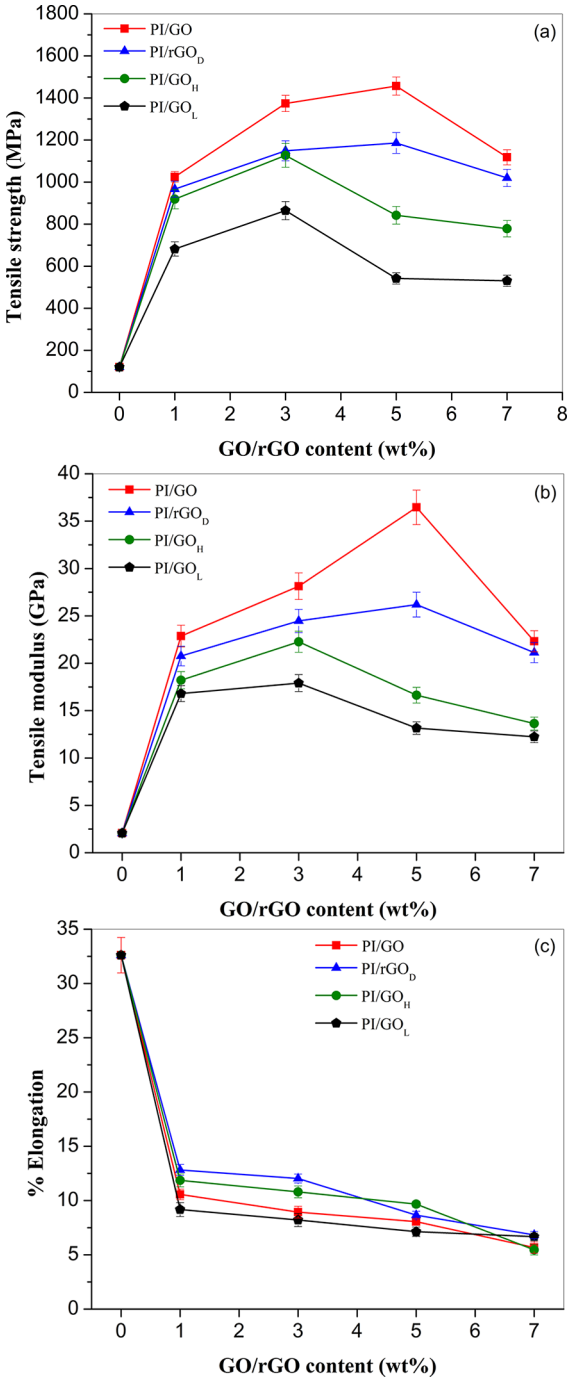

Figure 6. Variations of (a) tensile strength, (b) tensile modulus, and (c) percent elongation at break of the nanocomposites, as a function of GO and rGO content.

The incorporation of rGO sheets also enhanced the tensile strength and tensile modulus of the PI, whereas the extent of enhancement of the tensile properties is found to be less upon reinforcement of the rGO sheets compared to that of the GO (Figure 6). For instance, the incorporation of 3 wt % rGO_D, rGO_H, and rGO_L into the PI matrix increased the tensile strength from 120.3 to 1149, 1127, and 864.4 MPa, which is 19.5%, 22%, and 59% lower than those obtained with GO (i.e., 1374 MPa), respectively. The trend of the Young's modulus with the rGO sheets loading is similar to that of the tensile strength. These results suggest that the reinforcement efficiency

Table 1. Mechanical Properties of the Pure PI and Its Nanocomposites with GO and rGOs

sample	tensile strength (MPa)	% elongation	Young's modulus (GPa)
pure PI	120.3	32.61	2.069
PI/GO (1 wt %)	1025	10.57	22.87
PI/GO (3 wt %)	1374	8.93	28.13
PI/GO (5 wt %)	1457	8.06	36.46
PI/GO (7 wt %)	1118	5.67	22.32
PI/rGO_D (1 wt %)	966	12.82	20.76
PI/rGO_D (3 wt %)	1149	12.03	24.47
PI/rGO_D (5 wt %)	1186	8.66	26.19
PI/rGO_D (7 wt %)	1020	6.83	21.13
PI/rGO_H (1 wt %)	919	11.86	18.21
PI/rGO_H (3 wt %)	1127	10.8	22.27
PI/rGO_H (5 wt %)	842	9.67	16.63
PI/rGO_H (7 wt %)	778	5.46	13.64
PI/rGO_L (1 wt %)	682	9.17	16.80
PI/rGO_L (3 wt %)	864	8.21	17.91
PI/rGO_L (5 wt %)	542	7.13	13.16
PI/rGO_L (7 wt %)	531	6.67	12.24

of the individual GO sheets is higher than that of the rGO into the PI matrix. This is due to the higher concentration of polar functional groups (e.g., hydroxyl, epoxide, and carboxylic acid groups) on the pristine GO surface, which might facilitate better interfacial adhesion between GO and PI versus rGO.

The PI/rGO_D nanocomposites showed significant enhancement in both the tensile strength and tensile modulus as the rGO_D content increases from 1 wt % to 5 wt %, whereas the tensile properties decreased with further increased in filler content (7 wt %) (Figure 6), inferring an identical loading efficiency, as observed for the GO filler. However, the optimum loading efficiency for achieving the highest tensile properties was determined to be lower for rGO_H and rGO_L (i.e., 3 wt %) compared to those observed for GO and rGO_D. Hydrazine and LAA are stronger reducing agents than DMF; hence, the amount of residual functional groups in the rGO_H and rGO_L nanofillers might be lower than that in the rGO_D, and that makes them different with respect to the extent of noncovalent interactions with the PI chain and the subsequent state of dispersion in the polymer matrix. Moreover, the limitation of the enhancement in tensile strength and modulus of the nanocomposites containing highly reduced rGO_H and rGO_L nanofillers might be a consequence of the incomplete exfoliation of rGO sheets and/or some multilayer structure of the rGO sheets, as shown in the TEM images.

3.5. Thermal Properties. Thermal stability is one of the important properties of PI-based nanocomposites, because they are potentially high-performance engineering plastics. Inorganic fillers have been reported to improve the thermal stability of polymer composites, relative to the host polymer. Nonoxidative thermal degradation studies of PI/GO and PI/rGO nanocomposites were performed using thermogravimetric analysis (TGA), as shown in Figure 7. The presence of graphene sheets noticeably improves the thermal stability of the PI, as both the onset degradation temperature (T_{onset}) and maximum mass loss temperature (T_{max}) are shifted toward higher temperatures and the degradation rate becomes slower. Since the thermal degradation of a polymer begins with chain cleavage and radical formation, the carbon surface of graphene nanofillers in the nanocomposite might act as a radical scavenger to delay the

dx.doi.org/10.1021/am300999g | ACS Appl. Mater. Interfaces 2012, 4, 4623−4630

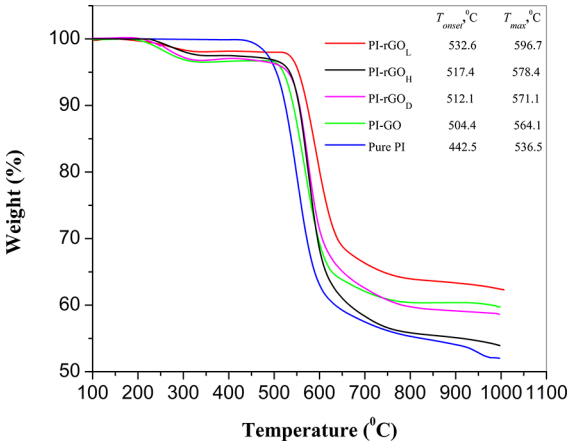

Figure 7. Thermogravimetric analysis (TGA) curves of nanocomposites with different GO and rGOs at a loading of 3 wt % in a N_2 atmosphere. T_{onset} and T_{max} respectively represent the onset degradation temperature where 3 wt % mass loss occurs and the maximum mass loss temperature where the maximum loss rate takes place.

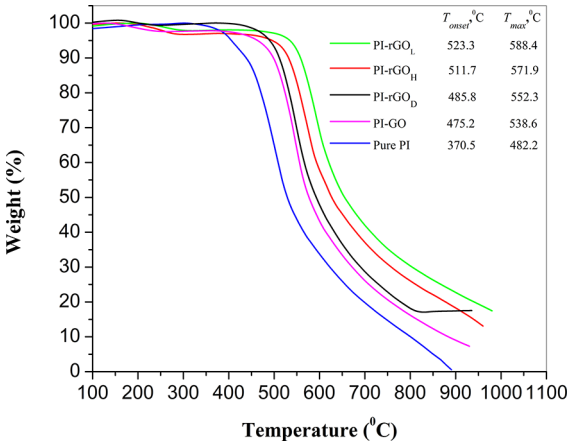

Figure 8. TGA curves of nanocomposites with different GO and rGOs at 3 wt % loading in an air atmosphere. T_{onset} and T_{max} respectively represent the onset degradation temperature where 3 wt % mass loss occurs and the maximum mass loss temperature where the maximum loss rate takes place.

onset of thermal degradation and, hence, improve the thermal stability of PI. In addition, the increased thermal stability of PI was attributed to the effect of a higher thermal conductivity of graphene sheets, which may facilitate heat dissipation within the polymer nanocomposite. The thermal degradation behavior of the PI/GO nanocomposite is almost identical to that of PI/rGO nanocomposites, consisting of an initial weight loss (~3%) at 220−310 °C, because of the removal of oxygen-containing functional groups present on the GO surface, followed by a major weight loss (~32%) between 490 °C and 650 °C, associated with decomposition of the PI matrix. The very small mass loss at 220−310 °C suggests that the GO/rGO sheets had been partially deoxygenated during the high-temperature treatment in the imidization step and the remaining small fraction of stable oxygen-containing groups on the resultant graphene sheets was removed during the TG heating scan. However, the higher degradation temperatures (T_{onset} and T_{max}) of the rGO-reinforced nanocomposites indicated their greater thermal stability, compared to the PI/GO nanocomposite. For the rGO sheets, the removal of thermally labile oxygen functional groups during chemical reduction causes a decrease in defect density (lower concentration of oxygen functionalities) and improves the thermal stability of graphene sheets to a large extent, which is consistent with the thermal behavior of PI/rGO nanocomposites. The decomposition of PI/GO$_L$ nanocomposite occurred at a substantially slower rate than that of the other rGO-reinforced nanocomposites, inferring its highest order of thermal stability.

Since the polymeric materials are commonly used under air conditions, it is much more important to investigate the effect of graphene sheets on thermal oxidation stability of the polymeric materials. As shown in Figure 8, the thermo-oxidative degradation of PI/graphene nanocomposites in an air atmosphere also has the same trend as those observed in a N_2 environment. The rGO-reinforced nanocomposites appear to be thermally more stable than PI/GO nanocomposites in an air atmosphere. The degradation temperatures (T_{onset} and T_{max}) of the nanocomposites are shifted toward lower temperatures, compared to those obtained under a N_2 atmosphere. However, the shifting was not more than 30 °C, inferring that graphene has great potential to enhance the thermal stability of PI in an oxidative atmosphere.

3.6. Electrical Conductivity. Pure PI is an insulating material with an electrical conductivity of ~10^{-15} S cm^{-1}.[28] Figure 9 shows that the incorporation of GO into the PI matrix

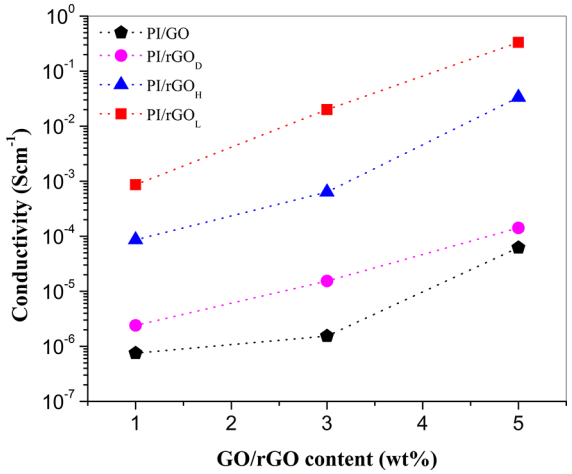

Figure 9. Electrical conductivity of PI/GO and PI/rGO nanocomposites, as a function of graphene loading.

results in an increase in electrical conductivity. This could be ascribed to higher electrical conductivity of the GO sheets (i.e., ~10^{-6} S cm^{-1}),[38,39] compared to a pure PI matrix. The electrical conductivities of the PI/GO and PI/rGO nanocomposites are summarized in Table 2. For example, a GO loading of 1 wt % results in an electrical conductivity of 7.51 × 10^{-7} S cm^{-1}, which is ~8 orders of magnitude higher than that of pure PI. The conductivity of the nanocomposite film continued to increase to 6.2 × 10^{-5} S cm^{-1} at a GO content of 5 wt %. This is attributed to the formation of conductive network through the PI matrix. Luong et al.[28] achieved an electrical conductivity of 8.9 × 10^{-7} S cm^{-1} by the incorporation of 0.75 wt % functionalized graphene sheets into PI. However, the graphene sheets obtained by the chemical reduction of graphene oxide are rather defective, and has a more pronounced effect on improving the electrical con-

dx.doi.org/10.1021/am300999g | ACS Appl. Mater. Interfaces 2012, 4, 4623−4630

Table 2. Electrical Conductivity of the PI Nanocomposites with GO and rGOs

sample	conductivity (S cm^{-1})
PI/GO (1%)	7.51×10^{-7}
PI/GO (3%)	1.54×10^{-6}
PI/GO (5%)	6.21×10^{-5}
PI/rGO_D (1%)	2.42×10^{-6}
PI/rGO_D (3%)	1.54×10^{-5}
PI/rGO_D (5%)	1.42×10^{-4}
PI/rGO_H (1%)	8.65×10^{-5}
PI/rGO_H (3%)	6.34×10^{-4}
PI/rGO_H (5%)	3.34×10^{-2}
PI/rGO_L (1%)	8.68×10^{-4}
PI/rGO_L (3%)	2.40×10^{-2}
PI/rGO_L (5%)	3.32×10^{-1}

ductivity of PI, compared to pristine GO. The conductivity of the nanocomposites achieved with different rGO fillers (5 wt %) are in the following order:

$$\text{PI/rGO}_D\ (1.42 \times 10^{-4}\ \text{S cm}^{-1}) < \text{PI/rGO}_H\ (3.34 \times 10^{-2}\ \text{S cm}^{-1}) < \text{PI/rGO}_L\ (3.42 \times 10^{-1}\ \text{S cm}^{-1})$$

The remarkably high electrical conductivity of the PI/rGO nanocomposites could be attributed to the effective recovery of the sp^2 network of carbon through chemical reduction and a good graphene particle-to-particle connection in the nanocomposites. rGO_L showed the maximum improvement in the electrical conductivity of PI, suggesting the efficient deoxygenation of GO with L-ascorbic acid. The conductivity of the PI/rGO_L nanocomposite increased sharply from 8.65×10^{-4} to 3.42×10^{-1} S cm^{-1} with increasing filler content from 1 wt % to 5 wt %, whereas limited enhancement was observed for the GO and rGO_D reinforced nanocomposites.

At a graphene content <1 wt %, the conductivity of the PI/GO or rGO nanocomposite films was $\sim 10^{-13}$ S cm^{-1}, which is comparable to that of neat PI. The conductivity of the nanocomposites gradually increased with increasing GO/rGO content (Figure 9), demonstrating a broad percolation transition. The conductivity percolation was not observed at lower graphene contents, probably because a graphene sheet loading of <1 wt % is too low to form a percolated network. The percolation theory has been used to describe the dependence of the electrical conductivity on filler volume content in the $\varphi > \varphi_c$ region. Above the conductivity percolation threshold, the electrical conductivity (σ) generally scales as a power law function:

$$\sigma \propto \sigma_0(\varphi - \varphi_c)^t \quad (1)$$

where σ_0 is the electrical conductivity of the fillers, φ the volume fraction of GO/rGO, φ_c the conductive percolation threshold (volume fraction), and t the scaling component, which depends on the dimensionality of the nanocomposite.[40] The percolation threshold is the critical content above which a continuous connected network is formed for the transport of electrons throughout the matrix. The experimental results are fitted by plotting $\log \sigma$ vs $\log(\varphi - \varphi_c)$. As shown in Figure 10, the conductivity of the PI/GO and PI/rGO_L nanocomposites agrees with the percolation behavior predicted by the power law equation (eq 1) with $\varphi_c \approx 0.0045$. From the linear fitting,

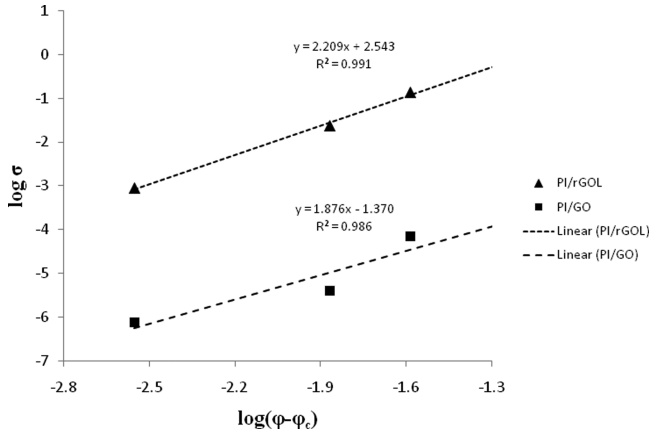

Figure 10. Fitting of the conductivity power law above the percolation threshold allowed estimation of the critical exponent (t).

the calculated critical exponent values of the PI/GO and PI/rGO_L nanocomposites are t = 1.87 and t = 2.20, respectively. The t values for both the PI/GO and PI/rGO_L nanocomposites are close to the value of 2, which is the theoretical value for the three-dimensional (3D) conducting network.[41]

4. CONCLUSIONS

In summary, we have demonstrated a simple and efficient method for the preparation of high-performance polyimide (PI) nanocomposites films reinforced with graphene oxide (GO) and different reduced graphene oxide (rGO) sheets. X-ray diffraction (XRD) and scanning electron microscopy (SEM) studies suggested well-dispersed exfoliated morphology of both types of chemically modified graphene sheets (GO and rGO) in a PI matrix, while transmission electron microscopy (TEM) observations indicated that the rGO retained stacked structure with a larger average thickness, compared to GO, possibly due to incomplete exfoliation. The addition of 5 wt % GO increased the tensile strength and tensile modulus to 1456.8 MPa and 36.46 GPa, respectively, corresponding to 12- and 18-fold increases, compared to pure PI, respectively. However, the extent of the improvement of the tensile properties after reinforcing the rGO sheets was inferior to that of GO. The superior mechanical properties of the GO sheets over rGO sheets might be related to the strong interfacial interactions between the polar functional groups of GO (or residual functional groups of rGOs) and PI matrix, which allow a high order of stress transfer from the matrix to the filler. The thermal stability of PI, under both nonoxidative and oxidative atmospheres, is significantly improved by the incorporation of graphene sheets. The rGOs render higher thermal stability of the nanocomposites, compared to GO. The highest thermal stability was achieved with rGO_L. The incorporation of chemically modified graphene significantly improved the electrical conductivity of PI, resulting in a sharp transition from an electrical insulator to a semiconductor. The electrical conductivity of the nanocomposites containing 5 wt % rGO_L was increased by 14 orders of magnitude, compared to that of pure PI, whereas the conductivity of the GO-reinforced nanocomposite was 10 orders of magnitude higher than that of PI.

AUTHOR INFORMATION

Corresponding Author

*Tel.: +82 53 950 5630. Fax: +82 53 950 6623. E-mail: psy@knu.ac.kr.

Author Contributions

§These authors contributed equally to this work.

Notes

The authors declare no competing financial interest.

ACKNOWLEDGMENTS

This work was supported by the National Research Foundation of Korea (NRF-2011-0020264).

REFERENCES

(1) Putz, K. W.; Palmeri, M. J.; Cohn, R. B.; Andrews, R.; Brinson, L. C. *Macromolecules* **2008**, *41*, 6752−6756.

(2) Bansal, A.; Yang, H.; Li, C.; Benicewicz, B. C.; Kumar, S. K.; Schadler, L. S. *J. Polym. Sci. Polym. Phys.* **2006**, *44*, 2944−2950.

(3) Putz, K.; Krishnamoorti, R.; Green, P. F. *Polymer* **2007**, *48*, 3540−3545.

(4) Fang, M.; Wang, K. G.; Lu, H. B.; Yang, Y. L.; Nutt, S. *J. Mater. Chem.* **2009**, *19*, 7098−7105.

(5) Hu, H. T.; Wang, X. B.; Wang, J. C.; Wan, L.; Liu, F. M.; Zheng, H.; Chen, R.; Xu, C. *Chem. Phys. Lett.* **2010**, *484*, 247−253.

(6) Kim, H.; Kobayashi, S.; AbdurRahim, M. A.; Zhang, M. L. J.; Khusainova, A.; Hillmyer, M. A.; Abdala, A. A.; Macosco, C. W. *Polymer* **2011**, *52*, 1837−1846.

(7) Lee, C.; Wei, X.; Kysar, J. W.; Hone, J. *Science* **2008**, *321*, 385−388.

(8) Balandin, A. A.; Ghosh, S.; Bao, W.; Calizo, I.; Teweldebrhan, D.; Miao, F.; Lau, C. N. *Nano Lett.* **2008**, *8*, 902−907.

(9) Dreyer, D. R.; Park, S.; Bielawski, C. W.; Ruoff, R. S. *Chem. Soc. Rev.* **2010**, *39*, 228−240.

(10) Li, D.; Muller, M. B.; Gilge, S.; Kaner, R. B.; Wallace, G. G. *Nat. Nanotechnol.* **2008**, *3*, 101−105.

(11) Schniepp, H. C.; Li, J. L.; McAllister, M. J.; Sai, H.; Herrera-Alonso, M.; Adamson, D. H.; Prud'homme, R. K.; Car, R.; Saville, D. A.; Aksay, I. A. *J. Phys. Chem. B* **2006**, *110*, 8535−8539.

(12) Zhu, Y. W.; Murali, S.; Stoller, M. D.; Velamakanni, A.; Piner, R. D.; Ruoff, R. S. *Carbon* **2010**, *48*, 2118−2122.

(13) Jiang, L.; Shen, X. P.; Wu, J. L.; Shen, K. C. *J. Appl. Polym. Sci.* **2010**, *118*, 275−279.

(14) Salavagione, H. J.; Martinez, G.; Gomez, M. A. *J. Mater. Chem.* **2009**, *19*, 5027−5032.

(15) Wang, X.; Yang, H.; Song, L.; Hu, Y.; Xing, W.; Lu, H. *Compos. Sci. Technol.* **2011**, *72*, 1−6.

(16) Rafiee, M. A.; Rafiee, J.; Wang, Z.; Song, H.; Yu, Z. Z.; Koratkar, N. *ACS Nano* **2009**, *3*, 3884−3890.

(17) Layek, R. K.; Samanta, S.; Chatterjee, D. P.; Nandi, A. K. *Polymer* **2010**, *51*, 5846−5856.

(18) Wissert, R.; Steurer, P.; Schopp, S.; Thomann, R.; Mülhaupt, R. *Macromol. Mater. Eng.* **2010**, *295*, 1107−1115.

(19) Jiayu, Z.; Dezhen, W.; Shengli, Q.; Zhanpeng, W. *J. Nanosci. Nanotechnol.* **2010**, *10*, 987−993.

(20) Faghihi, K.; Hajibeygi, M.; Shabanian, M. *Chin. Chem. Lett.* **2010**, *21*, 1387−1390.

(21) Min, C.-K.; Wu, T.-B.; Yang, W.-T.; Chen, C.-L. *Compos. Sci. Technol.* **2008**, *68*, 1570−1578.

(22) Tommalieh, M. J.; Zihlif, A. M. *Physica B. Condens. Mater.* **2010**, *405*, 4750−4754.

(23) Zhang, Y.-H.; Dang, Z.-M.; Fu, S.-Y.; Xin, J.-H.; Deng, J.-G.; Wu, J.; Yang, S.; Li, L.-F.; Yan, Q. *Chem. Phys. Lett.* **2005**, *401*, 553−557.

(24) Huang, H.-Y.; Huang, T.-C.; Yeh, T.-C.; Tsai, C.-Y.; Lai, C.-L.; Tsai, M.-H.; Yeh, J.-M.; Chou, Y.-C. *Polymer* **2011**, *52*, 2391−2400.

(25) Thuau, D.; Koutsos, V.; Cheung, R. *J. Vac. Sci. Technol. B.* **2009**, *27*, 3139−3144.

(26) Zhang, Y.; Xiao, S.; Wang, Q.; Liu, S.; Qiao, Z.; Chi, Z.; Xu, J.; Economy, J. *J. Mater. Chem.* **2011**, *21*, 14563−14568.

(27) Wei, Y. W.; Jianfei, C. J.; Chan-Park, M. B. *Chem. Mater.* **2011**, *23*, 4149−4157.

(28) Luong, N. D.; Hippi, U.; Korhonen, J. T.; Soininen, A. J.; Ruokolainen, J.; Johansson, L.-S.; Nam, J.-D.; Sinh, L. H.; Seppälä, J. *Polymer* **2011**, *52*, 5237−5242.

(29) Liu, H.; Li, Y.; Wang, T.; Wang, Q. *J. Mater. Sci.* **2012**, *47*, 1867−1874.

(30) Kim, G. Y.; Choi, M.-C.; Lee, D.; Ha, C.-S. *Macromol. Mater. Eng.* **2012**, *297*, 303−311.

(31) Chen, D.; Zhu, H.; Liu, T. *ACS Appl. Mater. Interfaces* **2010**, *2*, 3702−3708.

(32) Huang, T.; Lu, R.; Su, C.; Wang, H.; Guo, Z.; Liu, P.; Huang, Z.; Chen, H.; Li, T. *ACS Appl. Mater. Interfaces* **2012**, *4*, 2699−2708.

(33) Hummers, W. S.; Offeman, R. E. *J. Am. Chem. Soc.* **1958**, *80*, 1339−1339.

(34) Lamb, R. N.; Baxter, J.; Grunze, M.; Kong, C. W.; Unert, W. N. *Langmuir* **1988**, *4*, 249−256.

(35) Ai, K.; Liu, L.; Lu, L.; Cheng, X.; Huo, L. *J. Mater. Chem.* **2011**, *21*, 3365−3370.

(36) Liu, J.; Cheng, S. Z. D.; Harris, F. W.; Hsiao, B. S.; Gardner, K. H. *Macromolecules* **1994**, *27*, 989−996.

(37) Wang, J.-Y.; Yang, S.-Y.; Huang, Y.-L.; Tien, H.-W.; Chin, W.-K.; Ma, M.-C. *J. Mater. Chem.* **2011**, *21*, 13569−13575.

(38) Kim, C.-J.; Khan, W.; Park, S.-Y. *Chem. Phys. Lett.* **2011**, *511*, 110−115.

(39) Park, S.; An, J.; Piner, R. D.; Jung, I.; Yang, D.; Velamakanni, A.; Nguyen, S. T.; Ruoff, R. S. *Chem. Mater.* **2008**, *20*, 6592−6594.

(40) Zhang, H.-B.; Zheng, W.-G.; Yan, Q.; Yang, Y.; Wang, J.-W.; Lu, Z.-H.; Li, G.-Y.; Yu, Z.-Z. *Polymer* **2010**, *51*, 1191−1196.

(41) Bauhofer, W.; Kovacs, J. Z. *Compos. Sci. Technol.* **2009**, *69*, 1486−1498.